PNAS RESEARCH ARTICLE | APPLIED PHYSICAL SCIENCES OPEN ACCESS

Multiscale landscaping of droplet wettability on fibrous layers of facial masks

Sang Jin Park[a,b], Cho Hee Lee[a,b], Yeonji Kim[a], Jun Hyuk Ko[a], Taewoo Kim[a], Seong Jin Kim[a], Sahn Nahm[b], Hyesung Cho[a,1], and Myoung-Woon Moon[a,c,d,1]

Edited by David Weitz, Harvard University, Cambridge, MA; received June 3, 2022; accepted October 26, 2022

Liquid mobility is ubiquitous in nature, with droplets emerging at all size scales, and artificial surfaces have been designed to mimic such mobility over the past few decades. Meanwhile, millimeter-sized droplets are frequently used for wettability characterization, even with facial mask applications, although these applications have a droplet-size target range that spans from millimeters to aerosols measuring less than a few micrometers. Unlike large droplets, microdroplets can interact sensitively with the fibers they contact with and are prone to evaporation. However, wetting behaviors at the single-microfiber level remain poorly understood. Herein, we characterized the wettability of fibrous layers, which revealed that a multiscale landscape of droplets ranged from the millimeter to the micrometer scale. The contact angle (CA) values of small droplets on pristine fibrous media showed sudden decrements, especially on a single microfiber, owing to the lack of air cushions for the tiny droplets. Moreover, droplets easily adhered to the pristine layer during droplet impact tests and then yielding widespread areas of contamination on the microfibers. To resolve this, we carved nanowalls on the pristine fibers by plasma etching, which effectively suppressed such wetting phenomena. Significantly, the resulting topographies of the microfibers managed the dynamic wettability of droplets at the multiscale, which reduced the probability of contamination with impact droplets and suppressed the wetting transition upon evaporation. These findings for the dynamic wettability of fibrous media will be useful in the fight against infectious droplets.

microdroplet wettability | antidroplet fibers | facial masks | droplet impact resistance

Significance

Unlike large droplets, microdroplets interact sensitively with the fibers they contact and are prone to evaporation in facial mask applications, while data for droplet sizes from the previous test regime skewed even after the worldwide spread of COVID-19. Herein, we present the wettability characteristics of fibrous layers, which reveal a multiscale landscape of droplet wettability from the millimeter to the micrometer scales to improve the understanding of dynamic wetting behaviors of infectious droplets on fibrous media.

Depending on the delicate balance (1, 2) between the surface tension of a liquid (3) and the surface energy of the solid (4) it contacts (5), a liquid droplet can be spontaneously mobile (6) (e.g., wetting (7) or dewetting (8, 9) behaviors). This mobility is manifested in nature as superwettability for droplets at all scales (10, 11), which inspires mimicry of wettability management with a variety of artificial structures, including spreading (12, 13), rolling (14), jumping (15), and repelling (16) for diverse applications (17). In physics, extrinsic superhydrophobicity can originate from embedded air cushions at asperities where a droplet is located, and the wettability of which can be probed with the Cassie–Baxter model (18). In this model, a structured interface with trapped air can increase the contact angles (CAs), while the underlying roughness interferes with the determination of a baseline in CA measurements when the droplet size results in interactions on the scale of the roughness. For reliable characterization, large droplets with millimeter sizes (e.g., droplets over 3 μl are recommended) (19) have generally been employed with such surfaces, which also enables effortless determination of the baselines. To support this, we define a characteristic ratio denoted as $\boldsymbol{D} = D_d/D_f$, where D_d is the diameter of the test droplets, and D_f is the feature sizes of the underlying structures, thereby presenting a skewed distribution, i.e., $\boldsymbol{D} > 50$, for data from previous studies (details in *SI Appendix*, Note S1).

Surprisingly, in turn, such large droplets have been used to verify antidroplet performance of facial masks, wherein engineered materials (20) and structures (21) aim at superhydrophobicity to protect (22–24) human respiratory systems from infectious droplets that may load viruses after the worldwide COVID-19 spread (25, 26). Indeed, similar to the tests of bioinspired surfaces, large droplets ($D_d > 1$ mm, *SI Appendix*, Fig. S1) are generally employed with porous filter layers consisting of fibers. For example, when considering an outer layer of an N95-grade mask made of polypropylene (PP) microfibers with diameters of 15~20 μm, the test regime exists in $\boldsymbol{D} > 50$ (for simplicity, here, we approximate $D_f = 20$ μm) (27). Nevertheless, the important targets, i.e., oral fluids left behind by human activity (e.g., speaking and coughing) (28, 29), have been overlooked, the sizes of which are at the microscale (30, 31) (e.g., an aerosol is defined as 5 μm or smaller) (32). Such tiny droplets are comparable in size with the individual microfibers ($\boldsymbol{D} \sim 1$) and obviously do not experience as much of an air cushion effect; moreover, the evaporation-induced wetting dynamics (33) of a droplet on a single microfiber remain

Author affiliations: [a]Extreme Materials Research Center, Korea Institute of Science and Technology, Seoul 02792, Republic of Korea; [b]Department of Materials Science and Engineering, Korea University, Seoul 02841, Republic of Korea; [c]Korea Institute of Science and Technology - Sungkyunkwan University Carbon-Neutral Research Center, Sungkyunkwan University (SKKU), Suwon 16419, Republic of Korea; and [d]School of Chemical Engineering, Sungkyunkwan University (SKKU), Suwon 16419, Republic of Korea

Author contributions: S.J.P., S.N., H.C., and M.-W.M. designed research; S.J.P., C.H.L., Y.K., J.H.K., T.K., and S.J.K. performed research; S.J.P. and M.-W.M. contributed new reagents/analytic tools; S.J.P., C.H.L., Y.K., J.H.K., T.K., S.J.K., H.C., and M.-W.M. analyzed data; and S.J.P., S.J.K., S.N., H.C., and M.-W.M. wrote the paper.

The authors declare no competing interest.

This article is a PNAS Direct Submission.

[1]To whom correspondence may be addressed. Email: hcho@kist.re.kr or mwmoon@kist.re.kr

This article contains supporting information online at https://www.pnas.org/lookup/suppl/doi:10.1073/pnas.2209586119/-/DCSupplemental.

Published December 5, 2022.

poorly understood thus far, especially in the regime $D < 1$. To reveal these dynamics, we consider herein droplet wettability on fibrous layers over a broad regime ($100 > D > 0.1$) and extend the current test regime such that it involves the distributions of real infectious droplets and their dynamic wetting phenomena. In the multiscale landscape of wettability and mobility we present, sudden decreases in the CAs of droplets are monitored in the regime, $D < 10$, due to the reduced air cushion effect operating at this scale. In addition, such tiny droplets are sensitive to the environment and are pinned during evaporation. Consequently, impact droplets easily adhere to the pristine fibrous surfaces in N95 masks and leave behind a wide contamination area after evaporation. Alternatively, we propose a simple route for suppressing the adhesion and wetting transition of droplets by exploiting the advantages of air cushions in keeping the extrinsic hydrophobicity of the surface at the level of individual fibers. As a proof of concept, we introduce nanowall structures carved into the fibers of pristine N95 masks, which enhance hydrophobic characteristics and dewetting behaviors even in the regime $D \sim 0.1$. Significantly, our strategy improves the repellency of fibers with nanowall structures and reduces the probability of adhesion of impact droplets. The proposed method is simple and scalable for current materials and systems, thereby enabling superior hydrophobicity, even at the microscale, which is two orders of magnitude smaller than that of the pristine N95 case.

Results

Outer Layer as the Area of Interest for a Multiscale Landscape of Droplet Wettability. Fig. 1*A* depicts the layers of a commercial N95-grade mask consisting of fibrous media. We consider the outer layer, the area of interest for this study, for the reasons noted below. First, the environment that results from wearing a facial mask (34, 35) is reminiscent of a bombardment by droplets with varying sizes, including tiny droplets in the range $D < 10$, and the outer layer is exposed to this environment initially and more frequently than the other layers. Second, once a droplet sits on the surface of a mask, it may undergo evaporation, thereby shrinking to a size smaller than that of the microfiber diameter ($D < 1$) over time. Third, the multiscale test regime we set (i.e., $100 > D > 0.1$) enables simulation of internal filter layers whose targets are mostly very small droplets in the range $D < 1$. Finally, it is easy to observe dynamic wettability, e.g., repellency of impact droplets and evaporation-induced phenomena, on the outer layer because it is exposed to the outside and not hidden by other layers. Therefore, we selected the outer layer as the area of interest.

First, we set four observation frames OFs (see the four boxes in Fig. 1*A*) onto the outer layer of an N95 mask. They were designed by varying the scales with factors of 0.1 in a serial fashion (i.e., 5×5 mm^2, 500×500 μm^2, 50×50 μm^2, and 5×5 μm^2 for OF#1, OF#2, OF#3, and OF#4, respectively). Such OFs are useful for monitoring multiscale phenomena, as exemplified in our previous study (4). In this work, each OF enables droplet wettability characterization at the multiscale for which the fiber sizes are fixed, but their densities and directions vary. In the schematic illustration, five droplets (i.e., 1 mm, 100 μm, 10 μm, 5 μm, and 1 μm in diameter) are scaled with respect to the fixed diameter of a microfiber (D_f = 20 μm). Note that the first goal is to measure the CAs of droplets in each OF. For these experiments, we prepared two types of samples: i) the outer layer of a pristine N95 mask and ii) a nanowall-structured layer via plasma etching (*SI Appendix*, Note S2 and Fig. S2), and their morphologies are shown in the scanning electron microscopy (SEM) images in Fig. 1 *B* and *C*, respectively. At low magnification (OF#1), both samples showed arrays of rectangular dimples resulting from bonding of the nonwoven fibers. In OF#1, typical droplets with $D_d \sim$ 1 mm were movable and sometimes trapped into the dimples, with a surface that is relatively smooth and less porous (Movie S1 and *SI Appendix*, Fig. S4). Measuring CA values is not easy once a droplet has fallen into a dimple. In contrast, once a much larger droplet is placed onto the outer layer, it guarantees strong hydrophobicity via the Cassie state. In this regard, most studies of mask applications tend to verify superwettability with such large droplets in the skewed regime, $D > 50$. Significantly, we extend the current test regime to $D \sim 0.1$ (see high-magnification SEM images), whereby the microdroplets feature different wetting behaviors via evaporation on smooth and nanowall-structured fibers, as delineated below.

Multiscale Landscape of Droplet Wettability on Pristine Fibrous Media. Next, the pristine fibrous outer layer of an N95 mask is characterized at the multiscale, and some noticeable constraints of sessile droplets are highlighted in Fig. 2*A*. The measured CA values are plotted in Fig. 2*B* (details in *SI Appendix*, Note S3). In the results, the average CA value for the pristine layer in OF#1 was approximately 124.2°, which follows the Cassie–Baxter model

$$\cos\theta_C = f(\cos\theta_f + 1) - 1, \quad [1]$$

where θ_C is the measured CA at the Cassie state, and θ_f is the equilibrium CA measured on a flat surface (here, $\theta_f \sim 94.3°$, *SI Appendix*, Fig. S6). f is the solid fraction of the test layer in contact with such large droplets (>1 mm in OF#1), with an estimated $f \sim 0.47$. Notably, unlike those large droplets, small droplets ($D < 1$) on the smooth surface of a single microfiber perceive the underlying surface as flat, which leads to an $f \sim 1.0$ in OF#3 and OF#4. Consequently, it is rational to assume that the value of f in OF#2 is between 0.47 and 1.0, thereby decreasing the CA values in the regime as the average of 109.8° (*SI Appendix*, Fig. S7), which was smaller than that in OF#1. However, we found it challenging to measure the CAs of droplets ranging from 100 to 250 μm on the porous fibrous surface because such droplets are not spherical in shape, as shown in the insets of (Fig. 2*B* and *SI Appendix*, Fig. S8), owing to multiple constraints resulting from their contacts with random fibers. In this regime, the number and direction of contacting fibers can affect the shapes of the small droplets, whereby some droplets show imbibition and penetration into the porous layers over time. Moreover, the directional randomness of the individual fibers and the locations of droplets on the curved surfaces of the fiber could lead to biased observations in measuring the CA values in OF#3 and OF#4. These difficulties might explain why the multiscale landscape of droplet wettability has not been probed for mask applications thus far.

To clarify such difficulties and further pursue multiscale characterization, we designed experiments with a single PP microfiber, motivated by Duprat C. et al. (1), which in turn suited OF#3 and OF#4. With the detailed strategy to exclude the possibility of biased observation in the CA measurement (*SI Appendix*, Fig. S9), droplets in the regime $D \sim 1$ featured the average CA values of 85.9° on the microfiber (*SI Appendix*, Fig. S10), which was relatively smaller than the CA recorded for a flat PP surface (i.e., $\theta_f \sim 94.3°$). We find that such low CA values were caused by the evaporation that yielded pinning of the droplets at this scale since the CA values for droplets in OF#4 were much smaller than those in OF#3. As the humidity during the CA measurements was 30%, it was hard to stabilize the small droplets on the fibers. To avoid unstable conditions owing to rapid evaporation, we further performed wettability characterization via the measurements under

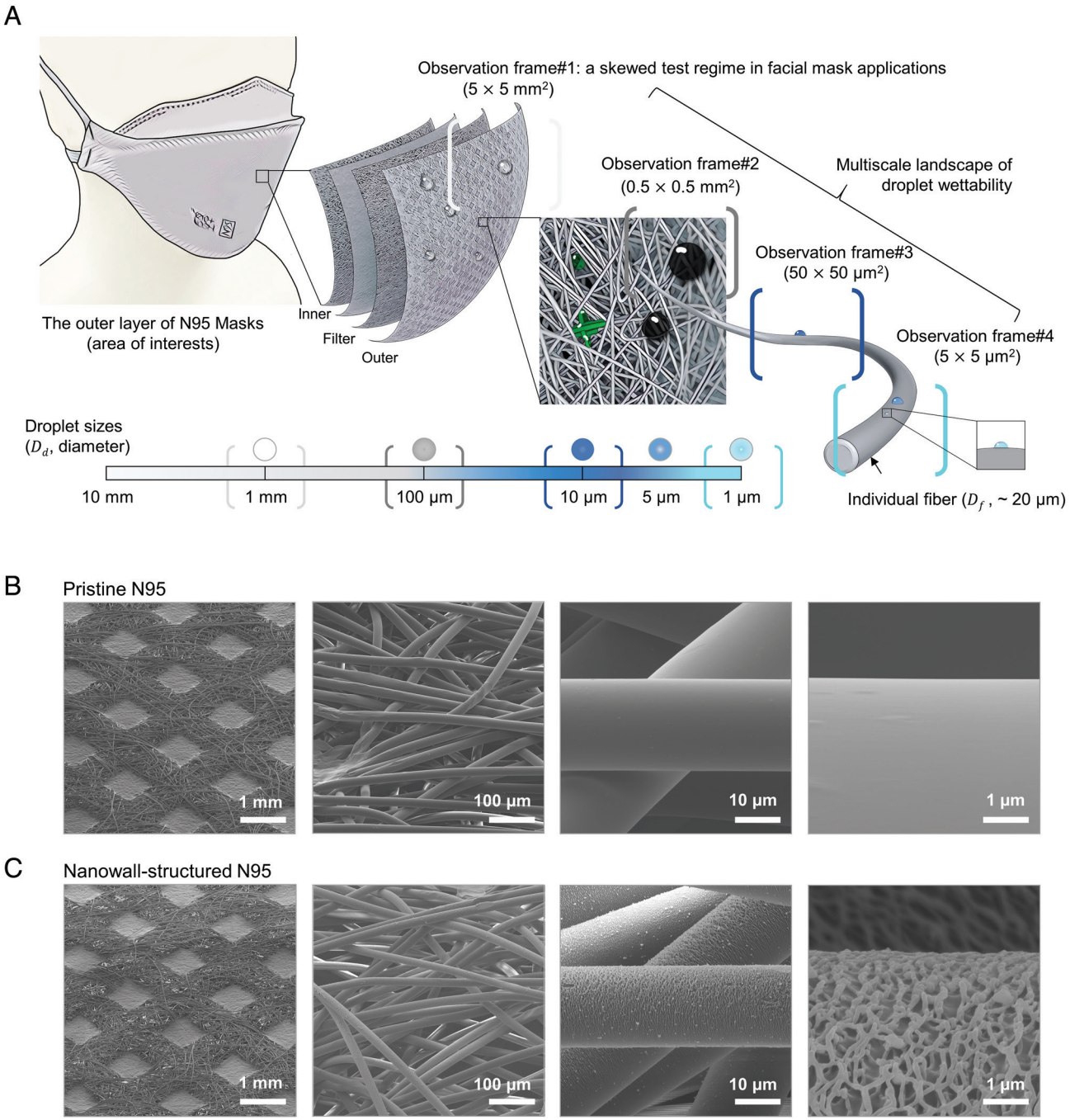

Fig. 1. (*A*) Layers of a 4-ply commercial N95 mask serving as the area of interest. Infectious droplets with a wide range of sizes are delivered to the outer layer, whereas the sizes of the droplets in previous studies were mostly larger than 1 mm. For a multiscale landscape, four OFs are set by using scales differing by a factor of 0.1. (*B* and *C*) SEM images in each OF exhibiting the outer layers of (*B*) a commercial N95 mask and (*C*) a modified layer with nanowall structures around each fiber. Notably, the two samples feature different wetting behaviors for small droplets.

extremely humid conditions in an environmental SEM (E-SEM, *SI Appendix,* Fig. S11) (>95% in the humidity) (36). Note that the CA values measured with the E-SEM system for the pristine layer (~ 87.3°) and the single strand were comparable (85.9° and 74.3° in OF#3 and OF#4, respectively), which revealed multiscale wettability with small droplets.

The measured values from the E-SEM experiments were similar to $\boldsymbol{\theta_f}$, suggesting that the value of f was close to 1.0 for those small droplets. Therefore, in the regime, the wetting may not hold with the Cassie state in Eq. 1, while it transitions into a wetting state with no air cushion available. On a facial mask, unless the surface of the pristine fibrous medium is not intrinsically strongly hydrophobic, the small infectious droplets after losing the air cushion may feature wetting behavior and pinning at this scale. To visualize this, we used nanoparticles as model virus particles to monitor the area of contamination after evaporation, wherein spreading or wicking by capillary action was observed, and a widespread area of contamination was eventually left behind (*SI Appendix,* Fig. S12). Previous tests (37) on flat surfaces with weak hydrophobicity indicated a similar tendency for the contaminated area formed via droplet evaporation, and this aspect, i.e., small infectious droplets behave as if the fiber had flat surfaces, is overlooked in the current wettability characterizations of porous fibrous layers for facial mask applications.

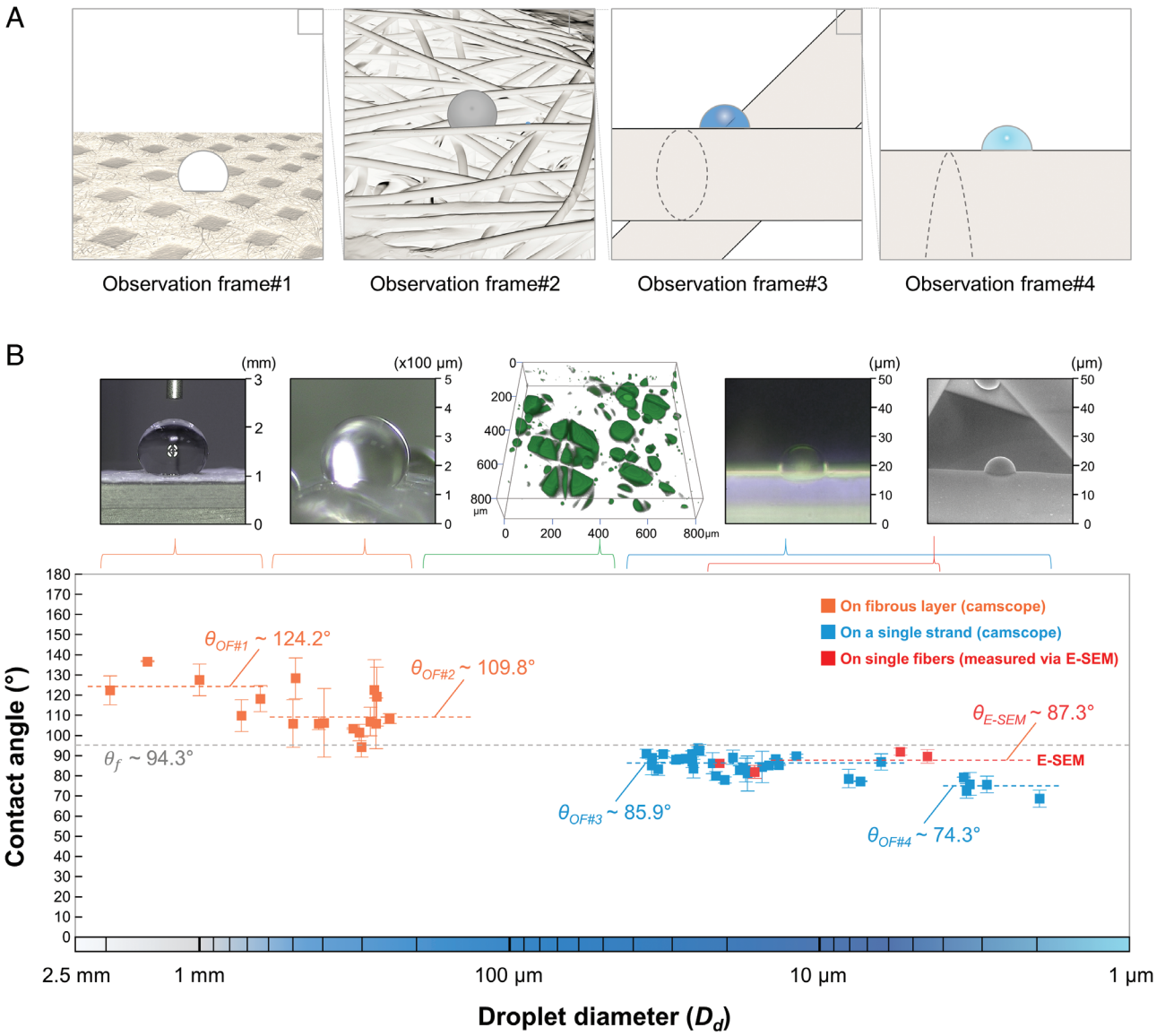

Fig. 2. (*A*) Basic phenomena for droplets on the pristine layer in the test regime. Unlike the dewetting behavior seen in OF#1, the small droplets wet in OF#2, OF#3, and OF#4 due to the reduced air cushion effects. (*B*) CA values measured in each OF, and the CA value decreases mostly in OF#3. Inset images appearing above the graph are the optical images (*Far Left* and *Left*), a confocal microscope image (*Middle*), a microscope image (*Right*), and an E-SEM image (*Far Right*).

A Route for Suppressing Wetting Transitions by Embedding Nanowall Structures into N95 Masks. As exemplified in nature, extrinsic hydrophobicity, assisted by the air cushion effect, can enhance droplet mobility. Thus far, a variety of materials and structures have been developed as internal filter layers of masks with enhanced hydrophobicity, but none of them has been subject to wettability characterization at the multiscale. Here, we probe the effectiveness of an additional hierarchy by carving pristine fibers at the nanoscale to dewet infectious droplets in $100 > D > 0.1$, as presented in Fig. 3. The primary mechanism for carving nanowall structures around PP microfibers involves coexistence of crystalline and amorphous phases in the fiber, as illustrated in Fig. 3*A*. It should be noted that these phases have different etching rates, as evidenced by X-ray diffraction (XRD) analyses, and the amorphous phase is much more easily etched than the crystalline phase (*SI Appendix,* Fig. S3*D*). In addition, since the plasma etches the fibers isotropically under low-vacuum conditions, the nanowall structures appear on the entire surfaces of fibers, even in the shadowed regions underneath adjacent microfibers (see the white box in Fig. 3*B*).

Armed with the nanowall structures, we improve the superhydrophobicity and suppress the wetting transition, as shown by the measured CA values plotted in Fig. 3*C*. Regardless of their sizes, the droplets exhibited high CA values across the OFs, and their shapes remained spherical. The wetting transitions that occurred in OF#2 and OF#3 for the pristine fibrous medium were not observed for the structured microfibers (*SI Appendix,* Figs. S13 and S14, respectively). To discuss the role of embedded roughness on the individual fibers, theoretically estimated CA values are provided in Fig. 3*C* for big and small droplets (i.e., $\theta_{T,\ big\ droplets}$ ~157.7° and $\theta_{T,\ small\ droplets}$~146.5°) (*SI Appendix,* Note S3). At the small scale (e.g., OF#3 and OF#4), the solid fraction of nanowalls can be measured as $f_{Nanowall} \sim 0.20$, and the small droplets remain in the Cassie state owing to the roughness, unlike droplets on a pristine microfiber. This roughness, in turn, greatly enhances the hydrophobicity to large droplets that are in contact with multiple fibers in OF#1 and OF#2, where the hierarchy leads to a small f value (i.e., $f = f_{Microfiber} \times f_{Nanowall} \sim 0.09$) and a high CA value (~157.7° in the Cassie–Cassie state) (38, 39). The differences in the dewetting states are illustrated in the insets of Fig. 3*C*.

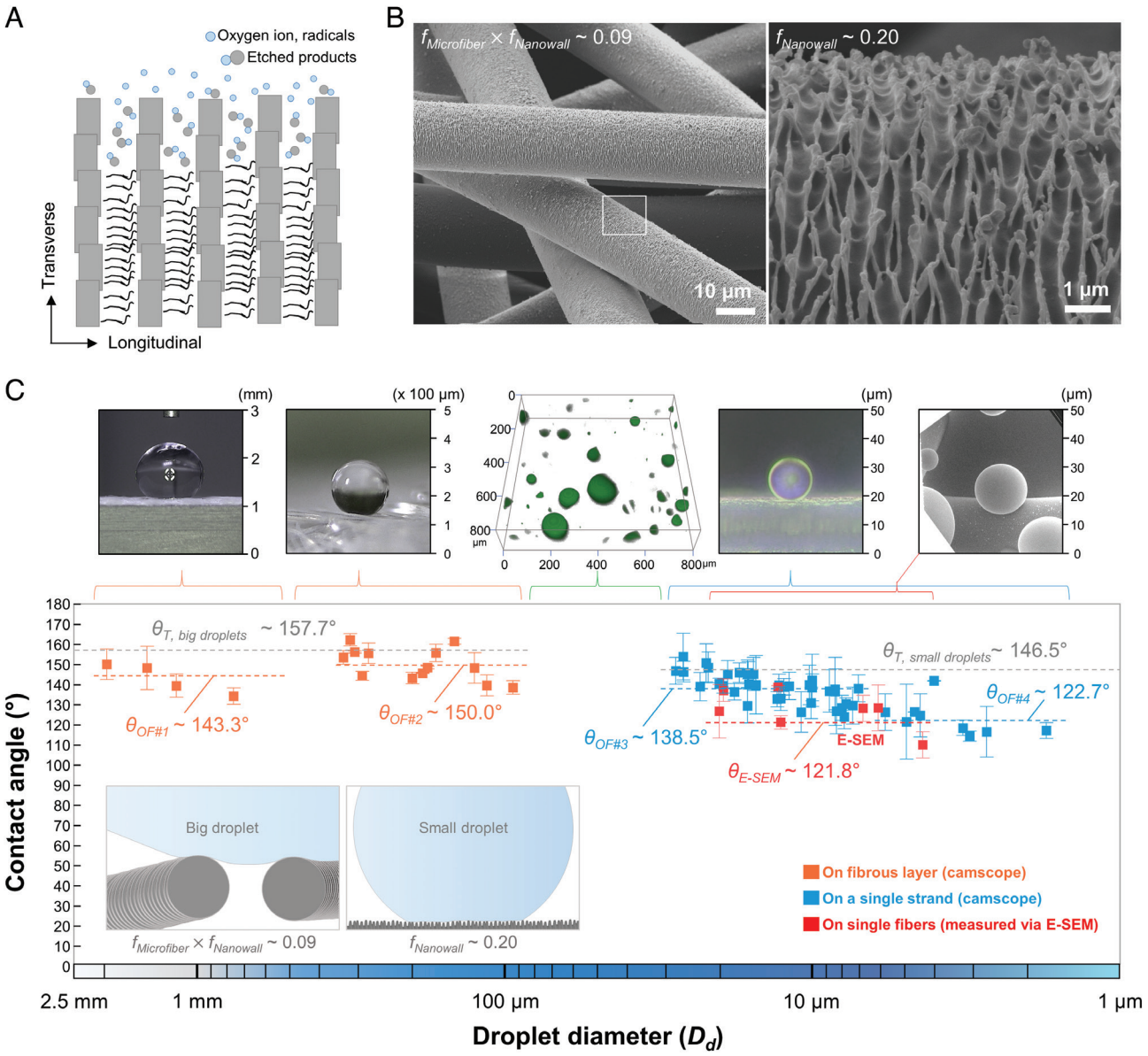

Fig. 3. (*A*) Mechanism for carving nanowall structures into the pristine layers of N95 masks. Spunbonded fibers exhibit coexistence of crystalline and amorphous phases on their surfaces, and the latter is etched easily via plasma treatment. (*B*) SEM images of fibrous media with structured microfibers. The area in the white box indicates a region of shadow, featuring structures due to low vacuum–assisted isotropic etching. (*C*) Dewetting behavior of droplets in the test regime and the measured CA values. Unlike the case of the pristine layer, this surface features extrinsic hydrophobicity even with droplets measuring a few micrometers in diameter. Inset images appearing above the graph are the optical images (*Far Left* and *Left*), the confocal microscope image (*Middle*), the optical image (*Right*), and the E-SEM image (*Far Right*). Schematic illustrations are inserted for the wetting state on the hierarchical (*Left*) and nanowalled (*Right*) surfaces.

Regarding the practical advantages of nanostructures, there is a two-step mechanism for reducing contamination during infectious droplet attacks. First, in addition to the large droplets, the smaller droplets in OF#2 and OF#3 do not easily adhere to the fibrous layer due to the high repellency of the surface (Movie S2). Second, once a droplet adheres to the fiber, the droplet remains spherical, which reduces the likelihood of virus immobilization because such contamination occurs by shear stresses after evaporation-induced pinning in the case of sessile droplets (40, 41). We note that even the tiny droplets in OF#4 exhibit spherical shapes (*SI Appendix,* Fig. S15) and display a sufficiently reduced area of contamination due to the dewetting behaviors of droplets on our nanowall-structured fiber surfaces (*SI Appendix,* Fig. S16).

Comparison of Droplet Mobilities at the Single-Microfiber Scale. The wetting transition mentioned for the droplets on a pristine fibrous medium is mainly based on evaporation, which has been discussed in previous studies (2, 37, 40, 41) of smooth surfaces, not individual fibers. Upon evaporation, a large droplet on a flat surface features two modes: i) the constant contact radius (CCR) mode and ii) the constant contact angle (CCA) mode, which retains characteristic paths over time. Recently, S. Shyam et al. (37) showed a mixed path involving both modes with a sessile droplet on a flat surface before late pinning (after 800 s with droplets with an initial volume of 1 μl). Our goal is to distinguish the pathways for dynamic wettability with small droplets on each pristine and structured fiber in the mixed mode to compare the mobility for $2.0 > D > 0.1$ (Fig. 4). To do this, the CA values were tracked by the radius of curvature, r, for a single droplet, as presented in Fig. 4 *A* and *B*.

For pristine fibers, the size of a droplet was decreased by evaporation ($2r \downarrow$) and then showed sudden pinning, resulting in an increment of $2r$ over that time. Then, the CA values decreased significantly where shear stress occurred internally. However, in

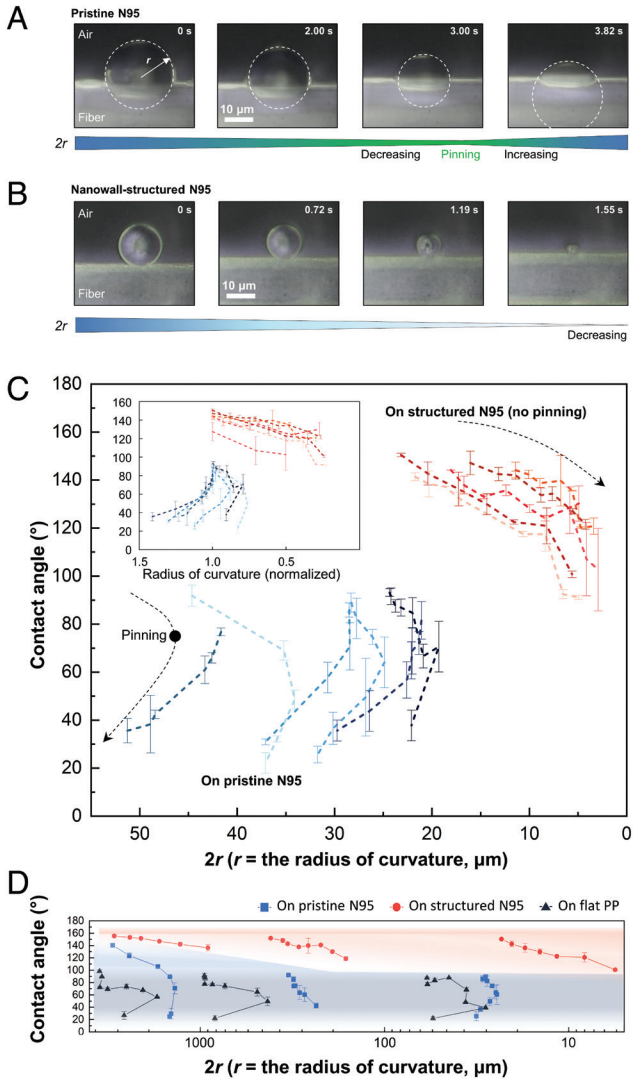

Fig. 4. (*A* and *B*) Observations of the dynamic wettability of droplets upon evaporation onto a single fiber, where (*A*) the droplet on the pristine fiber is pinned suddenly, unlike the case of a droplet (*B*) on the structured fiber. After pinning, shear stress–induced contamination occurs at the area of contact for the case of pristine layers. (*C*) Comparison of the dynamic wettability for both cases; CA values are plotted with respect to the value of 2r, and r is the radius of curvature. Pinning occurs when the CA is approximately 75°. (*D*) Dynamic wettability is explored with multiscale droplet diameters ranging from a few millimeters (D ~ 100) to a few micrometers (D ~ 0.1) by measuring the CA values, which are plotted with respect to the value of 2r upon evaporation.

the case of nanowall-structured fibers, the value of $2r$ decreased continuously until it reached the lower boundary of OF#4 (<2 μm in diameter). The correlation between $2r$ values and the CA values is presented in Fig. 4*C*. In detail, this suggests that once a droplet is evaporated and the CA reaches approximately 75°, pinning starts. However, for the structured fibers, the CA values exceeded 100° during evaporation, which caused suppression of the wetting transition. This dewetting phenomenon originated from the air cushion under the droplet in contact with the nanostructures. By normalizing the values of $2r$ with respect to the initial sizes of sessile droplets (an *Inset* in Fig. 4*C*), the two samples featured different routes for dynamic wettability. Moreover, such dewetting was consistently found for droplets on the nanowall-structured fibrous layers, which featured no pinning effect regardless of the droplet size in the test regime (see the data colored in red in Fig. 4*D*). In this way, the hierarchical structure–embedded fibers exhibited a universal dewetting phenomenon in the fibrous medium, suggesting the importance of embedded superhydrophobicity for fibrous outer layers in mask applications.

Dynamic Wettability of Impact Droplets on the Outer Surface of Masks. As mentioned above, the facial mask environment involves bombardment by infectious droplets; they impact the outer surface with momentum and act more dynamically than sessile droplets, as illustrated in Fig. 5*A* (experimental details in *SI Appendix*, Note S3 and Fig. S17). Interestingly, the droplets hitting the sample surfaces mostly exhibited the following four phenomena in our experiments, as shown in Fig. 5*B*: i) deposition of a droplet that adhered to the surface after hitting, ii) breakup deposition of a droplet that separated into small droplets and then adhered to the layer, iii) rebound, and iv) breakup rebound that occurred when the repellency of the surface was strong. By varying the velocity and the droplet size in the impact tests, we have obtained maps for the pristine and nanowall-structured layers (Fig. 5 *C* and *D*, respectively). Unlike the pristine surface, the nanowall-structured layer had a low CA hysteresis of 6.7° (*SI Appendix,* Fig. S18) and thus repelled the droplets in most tests, which would play a key role in protecting the outer layer from contamination by infectious droplets (Movie S3). A surface with low contact angle hysteresis (CAH) values repels droplets or undergoes dewetting upon evaporation as the kinetic barriers for moving contact lines are also low (42). We further tracked the very small droplets during the impact tests in OF#3 on the single strands without and with the nanostructures (*SI Appendix,* Fig. S19 and Movie S4).

It is well known that a liquid-coated surface may have different wettability than a dry solid surface when liquid droplets start to accumulate on the solid surface (43, 44). We observed that the impact of droplets yielded wetting of the pristine surface via either deposition or breakup deposition, which resulted in pinned droplets on the fibrous layer (45). This constraint enhances the likelihood of droplet adhesion and accumulation when they hit the same or nearby locations repeatedly, which eventually increases the size of the accumulated droplet (i) of Fig. 5*E* and Movie S5). This suggests that the air cushion effect of the pristine fibrous layer is easily diminished due to the wetting effects of droplets, which in turn provides the potential of leaving a large area of contamination after evaporation. On the other hand, the nanowall structures can inhibit wetting and pinning of droplets even in the multiple impact tests, making the air cushion effect robust and repeatable (ii) of Fig. 5*E* and Movie S5). Although a droplet adheres to the fibrous layer with nanowalls and makes a residue during multiple impact events in our tests (see the impact events N = 30th and 42nd in Movie S5), another impacting droplet (N = 34th and 43rd) can take the residue off from the surface, respectively, maintaining the surface clean. This aspect indicates that the strong resistance to impacting droplets is realized on the commercial N95 mask surface via our plasma-etching strategy. Such functions (i.e., abilities to repel or self-clean the droplets against impact) on surfaces are of significance in some species of living creatures (insects and plants) (10), which is adequately mimicked in this work for such practical aspects successfully.

Conclusion

We have presented a multiscale landscape for droplet wettability and mobility onto N95 masks and their structural derivatives to discuss the potential for avoiding adhesion of infectious droplets and contamination of mask surfaces via evaporation. A test regime that was excluded in previous studies was probed by using a single strand for the wettability characterization, which extended the test regime down to D ~ 0.1. Our multiscale landscape for the pristine

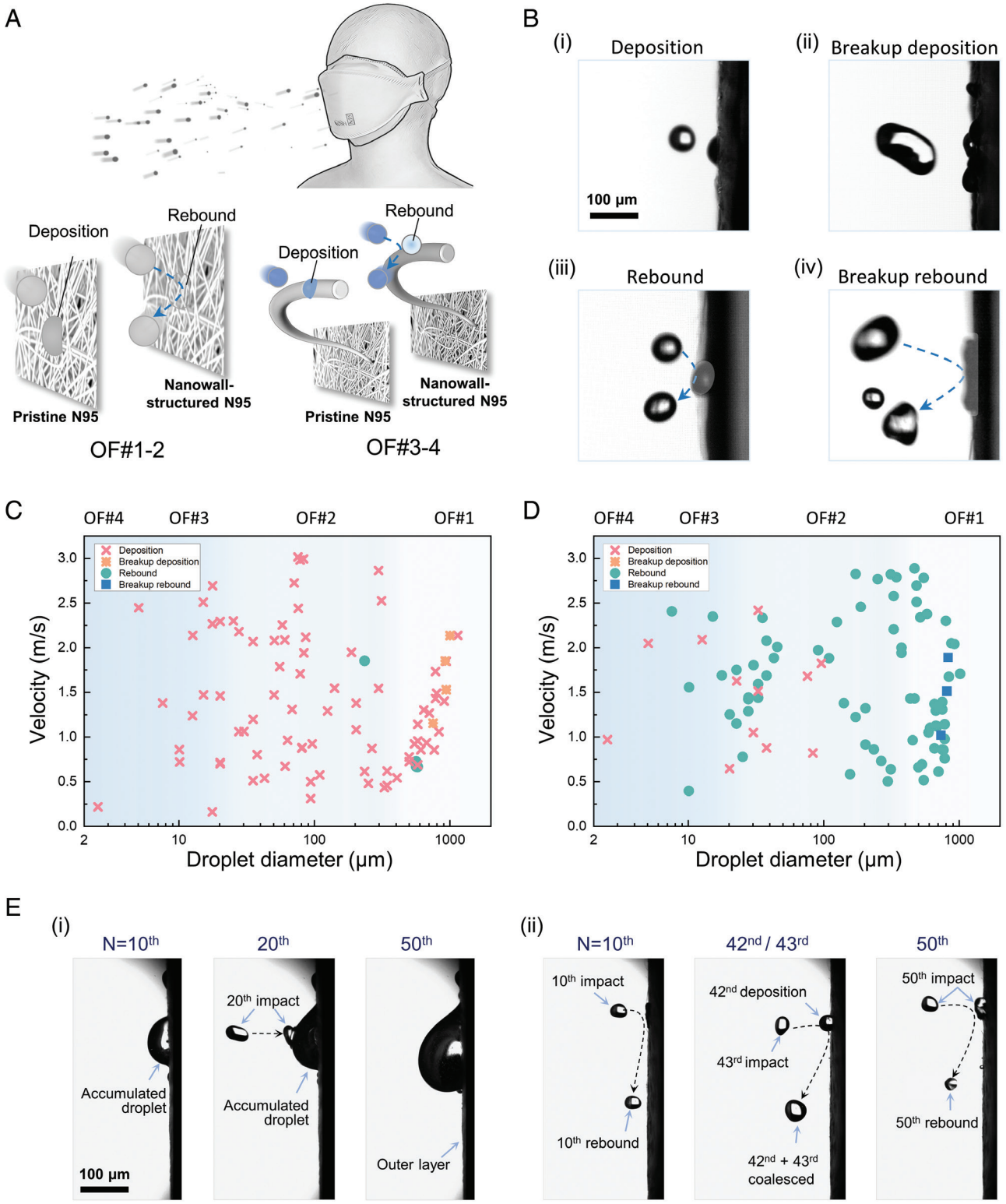

Fig. 5. (*A*) Schematic describing the droplet impact tests used with facial mask fibrous layers (OF#1 and OF#2) and single fibers (OF#3 and OF#4). (*B*) Four possible scenarios after droplet impact on test surfaces: (*i*) deposition, (*ii*) breakup and deposition, (*iii*) complete rebound, and (*iv*) breakup and rebound. (*C* and *D*) Droplet impact regime maps with water droplets at the multiscale on the pristine N95 face mask (*C*) and nanowall-structured (*D*) layers. For the pristine layer, deposition and breakup deposition of impact droplets occur frequently, while the nanostructured fibers mostly feature rebound and breakup rebound in the impact tests. (*E*) Digital images showing multiple droplets impacting the same location up to 50 times: Multiple droplets were piled up on the pristine layer (*i*), while each droplet rebounded consistently against the nanowall-structured layer (*ii*). N represents the number of the droplet impacting event against the surface in succession.

fibrous medium revealed a sudden wetting transition for droplets with CA values smaller than 90° when the size of the droplet was comparable with the diameter of the microfiber during evaporation. This wetting transition has the potential to contaminate the smooth surfaces of fibers in the regime $1 > D > 0.1$. This dynamic wettability is currently overlooked in the field for mask

applications, and we presented a route for circumventing contamination by enhancing hydrophobicity. To achieve this, the coexistence of crystalline and amorphous phases in the PP microfibers was exploited by conducting plasma etching, which led to the embedment of nanowall structures around each fiber. The structured fibrous medium suppressed the wetting transition with robust air cushion effects, and the droplet wetting dynamics during evaporation were visualized by tracking the CA values and the radii of curvature in real time. Moreover, this effect significantly reduced the adhesion of the impacting droplets, which is important for reducing contamination of mask surfaces by infectious droplets. The strategy presented is made scalable, reliable, and practical with the use of current plasma processes (*SI Appendix*, Figs. S20 and S21 (46)), which will help develop to ensure effective mask clearing of infectious droplets in the future.

Materials and Methods

Sample Preparation. Nonwoven, PP, spunbonded fabrics from the outer layer of an N95-type respirator (referred to as the N95 mask) (9210 + Aura, 3M, U.S.A.) were used. The outer ply of the N95 mask was composed of PP fibers with diameters of 15~20 μm. For the pristine case, a specimen was prepared by cutting the outer layer into 20 × 20-mm^2 pieces prior to wettability characterization. To prepare a layer of nanowall-structured microfibers, the whole outer layer of an N95 mask was brought inside a chamber for plasma treatment. Prior to plasma etching, the outer layer of the N95 mask was cleaned by N_2 gas to remove dust and then placed on a cathode using an insulated fixture. RF–glow discharge plasma treatments were conducted with a power of 55 W and a bias voltage of 250 ± 10 V under 200 ± 10 mTorr working pressures. The oxygen gas flow rate was set at 40 sccm for 30 min of treatment. Hexamethyldisiloxane (HMDSO; Sigma Aldrich) was coated for 1 min at 10 W under 20 mTorr, rendering the surface superhydrophobic. The droplet impact test was performed by controlling the droplet size and velocity with the opening time and gas regulator–assisted injection pressure of the piezo-actuated droplet dispenser (Nordson PICO Pμlse, U.S.A.). The droplet images were recorded with a high-speed camera operating at 4,000~8,000 frames per second (Photron Mini UX high-speed camera, Japan).

Characterization. The surfaces of the pristine and nanowall-structured samples were observed by the field emission scanning electron microscopy (FE-SEM, Regulus 8230; Hitachi, Japan). Surfaces were covered with a 5-nm PtPd film prior to observation. For wettability characterization, a CA goniometer (100-00-115; Ramé-hart Instrument Co., U.S.A.) was used. A customized CA measurement setup was prepared. We observed wetting behaviors using laser scanning confocal microscopy (LSCM). We used an inverted-type scanning confocal microscope (SP8 FALCON; Leica Microsystems, Germany) with a 20× objective lens. These analyses were performed at the KBSI, Daegu Center, Republic of Korea. We used a picosecond laser line (488 nm) as the excitation source. A hybrid photon detector collected fluorescence data at wavelengths of 500~700 nm from droplets sprayed on nonwoven fiber fabrics (the outer layer of N95). The DI water droplets were dyed with a 10 μM rhodamine 123 aqueous solution. Confocal fluorescence images of 512 × 512 pixels were recorded using a Z-Galvo stage. 2D and 3D images were constructed by using the Leica software (LAS X Ver.3.5.2). E-SEM analyses were performed using a Quattro S (Thermo Fisher Scientific, U.S.A.) to compare the wetting behaviors in OF#3 and OF#4. A Peltier cold stage was installed to condense water vapor on the surfaces of the substrates. The working distances were 5~7 mm, and the acceleration voltages were 5~10 kV. To cool the surfaces of the substrates, we maintained conditions of 700 Pa and 2°C for 30 min. Then, we investigated the wetting behaviors while increasing the pressure from 700 Pa to 1,000 Pa.

Data, Materials, and Software Availability. All study data are included in the article and/or *SI Appendix*.

ACKNOWLEDGMENTS. This work was supported by the Korea Coast Guard, Korea (KIMST-20210584). The authors also acknowledge support from a KIST internal project (2E31790). This research was supported by the Research Program to Solve Urgent Safety Issues of the National Research Foundation of Korea (NRF) funded by the Korean government (Ministry of Science and ICT (MSIT)) (no. 2020M3E9A1113568).

1. C. Duprat, S. Protière, A. Y. Beebe, H. A. Stone, Wetting of flexible fibre arrays. *Nature* **482**, 510–513 (2012).
2. J. Gerber, T. Lendenmann, H. Eghlidi, T. M. Schutzius, D. Poulikakos, Wetting transitions in droplet drying on soft materials. *Nat. Commun.* **10**, 1–10 (2019).
3. V. G. Levich, V. S. Krylov, Surface-tension-driven phenomena. *Annu. Rev. Fluid Mech.* **1**, 293–316 (1969).
4. J. Kim *et al.*, Nonlinear frameworks for reversible and pluripotent wetting on topographic surfaces. *Adv. Mater.* **29**, 1605078 (2017).
5. N. Gao *et al.*, How drops start sliding over solid surfaces. *Nat. Phys.* **14**, 191–196 (2018).
6. T. S. Wong *et al.*, Bioinspired self-repairing slippery surfaces with pressure-stable omniphobicity. *Nature* **477**, 443–447 (2011).
7. M. Rauscher, S. Dietrich, Wetting phenomena in nanofluidics. *Annu. Rev. Mater. Res.* **38**, 143–172 (2008).
8. H. Cho *et al.*, Replication of flexible polymer membranes with geometry-controllable nano-apertures via a hierarchical mould-based dewetting. *Nat. Commun.* **5**, 1–10 (2014).
9. A. M. J. Edwards, R. Ledesma-Aguilar, M. I. Newton, C. V. Brown, G. McHale, Not spreading in reverse: The dewetting of a liquid film into a single drop. *Sci. Adv.* **2**, e1600183 (2016).
10. M. Liu, S. Wang, L. Jiang, Nature-inspired superwettability systems. *Nat. Rev. Mater.* **2**, 1–17 (2017).
11. Y. Lu *et al.*, Robust self-cleaning surfaces that function when exposed to either air or oil. *Science* **347**, 1132–1135 (2015).
12. N. A. Dudukovic *et al.*, Cellular fluidics. *Nature* **595**, 58–65 (2021).
13. D. Bonn, J. Eggers, J. Indekeu, J. Meunier, Wetting and spreading. *Rev. Mod. Phys.* **81**, 739–805 (2009).
14. Y. Y. Yan, N. Gao, W. Barthlott, Mimicking natural superhydrophobic surfaces and grasping the wetting process: A review on recent progress in preparing superhydrophobic surfaces. *Adv. Colloid Interface Sci.* **169**, 80–105 (2011).
15. N. Miljkovic *et al.*, Jumping-droplet-enhanced condensation on scalable superhydrophobic nanostructured surfaces. *Nano Lett.* **13**, 179–187 (2013).
16. J. C. Bird, R. Dhiman, H.-M. Kwon, K. K. Varanasi, Reducing the contact time of a bouncing drop. *Nature* **503**, 385–388 (2013).
17. H. J. Cho, D. J. Preston, Y. Zhu, E. N. Wang, Nanoengineered materials for liquid-vapour phase-change heat transfer. *Nat. Rev. Mater.* **2**, 1–17 (2016).
18. A. B. D. Cassie, S. Baxter, Wettability of porous surfaces. *Trans. Faraday Soc.* **40**, 546–551 (1944).
19. T. Huhtamäki, X. Tian, J. T. Korhonen, R. H. A. Ras, Surface-wetting characterization using contact-angle measurements. *Nat. Protoc.* **13**, 1521–1538 (2018).
20. A. Kumar *et al.*, Copper@ZIF-8 core-shell nanowires for reusable antimicrobial face masks. *Adv. Funct. Mater.* **31**, 2008054 (2021).
21. N. El-Atab *et al.*, Flexible nanoporous template for the design and development of reusable anti-COVID-19 hydrophobic face masks. *ACS Nano* **14**, 7659–7665 (2020).
22. Z. Tang *et al.*, A materials-science perspective on tackling COVID-19. *Nat. Rev. Mater.* **5**, 847–860 (2020).
23. A. Tuñón-Molina *et al.*, Protective face masks: Current status and future trends. *ACS Appl. Mater. Interfaces* **13**, 56725–56751 (2021).
24. M. Karmacharya, S. Kumar, O. Gulenko, Y. K. Cho, Advances in facemasks during the COVID-19 pandemic era. *ACS Appl. Bio Mater.* **4**, 3891–3908 (2021).
25. S. Kumaran, E. Oh, S. Han, H. J. Choi, Photopolymerizable, universal antimicrobial coating to produce high-performing, multifunctional face masks. *Nano Lett.* **21**, 5422–5429 (2021).
26. M. Choi *et al.*, Functionalized polyurethane-coated fabric with high breathability, durability, reusability, and protection ability. *Adv. Funct. Mater.* **31**, 2101511 (2021).
27. H. Zhong *et al.*, Reusable and recyclable graphene masks with outstanding superhydrophobic and photothermal performances. *ACS Nano* **14**, 6213–6221 (2020).
28. S. N. Rogak *et al.*, Properties of materials considered for improvised masks. *Aerosol Sci. Technol.* **55**, 398–413 (2021).
29. M. Abkarian, S. Mendez, N. Xue, F. Yang, H. A. Stone, Speech can produce jet-like transport relevant to asymptomatic spreading of virus. *Proc. Natl. Acad. Sci. U.S.A.* **117**, 25237–25245 (2020).
30. R. Zhang, Y. Li, A. L. Zhang, Y. Wang, M. J. Molina, Identifying airborne transmission as the dominant route for the spread of COVID-19. *Proc. Natl. Acad. Sci. U.S.A.* **117**, 14857–14863 (2020).
31. D. A. Edwards *et al.*, Exhaled aerosol increases with COVID-19 infection, age, and obesity. *Proc. Natl. Acad. Sci. U.S.A.* **118**, 1–6 (2021).
32. J. Gralton, E. Tovey, M. L. McLaws, W. D. Rawlinson, The role of particle size in aerosolised pathogen transmission: A review. *J. Infect.* **62**, 1–13 (2011).
33. Z. He *et al.*, Droplet evaporation residue indicating SARS-COV-2 survivability on surfaces. *Phys. Fluids* **33**, 013309 (2021).
34. J. Xi, X. A. Si, R. Nagarajan, Effects of mask-wearing on the inhalability and deposition of airborne SARS-CoV-2 aerosols in human upper airway. *Phys. Fluids* **32**, 123312 (2020).
35. J. Howard *et al.*, An evidence review of face masks against COVID-19. *Proc. Natl. Acad. Sci. U.S.A.* **118**, 1–12 (2021).
36. Q. F. Wei, R. R. Mather, A. F. Fotheringham, R. D. Yang, ESEM study of wetting of untreated and plasma treated polypropylene fibers. *J. Ind. Text.* **32**, 59–66 (2002).
37. S. Shyam, P. K. Mondal, S. Wongwises, Survivability of a particle laden sessile coughed and sneezed droplet subjected to different ambient conditions. *Int. J. Therm. Sci.* **176**, 107525 (2022).
38. Y. Rahmawan, M. W. Moon, K. S. Kim, K. R. Lee, K. Y. Suh, Wrinkled, dual-scale structures of diamond-like carbon (DLC) for superhydrophobicity. *Langmuir* **26**, 484–491 (2010).
39. M. S. Bell, A. Shahraz, K. A. Fichthorn, A. Borhan, Effects of hierarchical surface roughness on droplet contact angle. *Langmuir* **31**, 6752–6762 (2015).
40. R. Bhardwaj, A. Agrawal, Likelihood of survival of coronavirus in a respiratory droplet deposited on a solid surface. *Phys. Fluids* **32**, 061704 (2020).

41. S. Kumar, H. P. Lee, The perspective of fluid flow behavior of respiratory droplets and aerosols through the facemasks in context of SARS-CoV-2. *Phys. Fluids* **32**, 111301 (2020).
42. L. Gao, T. J. McCarthy, Contact angle hysteresis explained. *Langmuir* **22**, 6234–6237 (2006).
43. C. Dorrer, J. Rühe, Condensation and wetting transitions on microstructured ultrahydrophobic surfaces. *Langmuir* **23**, 3820–3824 (2007).
44. S. Bagchi, S. Basu, S. Chaudhuri, A. Saha, Penetration and secondary atomization of droplets impacted on wet facemasks. *Phys. Rev. Fluids* **6**, 110510 (2021).
45. Y. Liu, X. Yan, Z. Wang, Droplet dynamics on slippery surfaces: Small droplet, big impact. *Biosurf. Biotribol.* **5**, 35–45 (2019).
46. Y. A. Lee *et al.*, Slippery, water-infused membrane with grooved nanotrichomes for lubricating-induced oil repellency. *Adv. Sci.* **9**, e2103950 (2022).